ALMA suggests outflows in $z \sim 5.5$ galaxies

S. Gallerani,[1]* A. Pallottini,[1,2,3] C. Feruglio,[1] A. Ferrara,[1] R. Maiolino,[2,3]
L. Vallini,[4,5,6] D. A. Riechers[7] and R. Pavesi[7]

[1]*Scuola Normale Superiore, Piazza dei Cavalieri 7, I-56126 Pisa, Italy*
[2]*Kavli Institute for Cosmology, University of Cambridge, Madingley Road, Cambridge CB3 0HA, UK*
[3]*Cavendish Laboratory, University of Cambridge, 19 J. J. Thomson Ave, Cambridge CB3 0HE, UK*
[4]*Nordita, KTH Royal Institute of Technology and Stockholm University, Roslagstullsbacken 23, SE-106 91 Stockholm, Sweden*
[5]*Istituto Nazionale di Astrofisica – Osservatorio Astronomico di Bologna, via Ranzani 1, I-40127 Bologna, Italy*
[6]*Dipartimento di Fisica e Astronomia, Universitá di Bologna, viale Berti Pichat 6/2, I-40127 Bologna, Italy*
[7]*Department of Astronomy, Cornell University, 220 Space Sciences Building, Ithaca, NY 14853, USA*

ABSTRACT

We present the first attempt to detect outflows from galaxies approaching the Epoch of Reionization (EoR) using a sample of nine star-forming (SFR $= 31 \pm 20\,\mathrm{M_\odot\,yr^{-1}}$) $z \sim 5.5$ galaxies for which the [C II]158 µm line has been previously obtained with Atacama Large Millimeter Array (ALMA). We first fit each line with a Gaussian function and compute the residuals by subtracting the best-fitting model from the data. We combine the residuals of all sample galaxies and find that the total signal is characterized by a flux excess of $\sim$0.5 mJy extended over $\sim$1000 km s^{-1}. Although we cannot exclude that part of this signal is due to emission from faint satellite galaxies, we show that the most probable explanation for the detected flux excess is the presence of broad wings in the [C II] lines, signatures of starburst-driven outflows. We infer an average outflow rate of $\dot{M} = 54 \pm 23\,\mathrm{M_\odot\,yr^{-1}}$, providing a loading factor $\eta = \dot{M}/\mathrm{SFR} = 1.7 \pm 1.3$ in agreement with observed local starbursts. Our interpretation is consistent with outcomes from zoomed hydrosimulations of Dahlia, a $z \sim 6$ galaxy (SFR $\sim 100\,\mathrm{M_\odot\,yr^{-1}}$), whose feedback-regulated star formation results into an outflow rate $\dot{M} \sim 30\,\mathrm{M_\odot\,yr^{-1}}$. The quality of the ALMA data is not sufficient for a detailed analysis of the [C II] line profile in individual galaxies. Nevertheless, our results suggest that starburst-driven outflows are in place in the EoR and provide useful indications for future ALMA campaigns. Deeper observations of the [C II] line in this sample are required to better characterize feedback at high-z and to understand the role of outflows in shaping early galaxy formation.

Key words: galaxies: evolution – galaxies: high-redshift – galaxies: ISM.

1 INTRODUCTION

Massive stars profoundly affect the interstellar medium (ISM) of galaxies by injecting energy and momentum in the gas. This occurs via radiation pressure, stellar winds, photoionization and supernovae (SNe, Dekel & Silk 1986; Mac Low & Ferrara 1999; Murray, Ménard & Thompson 2011). As a result the gas is heated and ionized, and it becomes turbulent. Moreover, a substantial fraction of the ISM can be cast into the halo (Hopkins, Quataert & Murray 2012; Pallottini, Gallerani & Ferrara 2014b; Liang, Kravtsov & Agertz 2016) and the intergalactic medium (IGM), thus enriching these components with freshly produced heavy elements (Oppenheimer & Davé 2006; Pallottini et al. 2014a). Outflows also play a key role in the life cycle of galaxies, as they control star

formation by regulating the amount of gas available to form stars. On cosmological scales, outflows are thought to shape the faint end of the galaxy luminosity function up to the highest redshifts at which galaxies can be observed (Dunlop 2013; Bouwens et al. 2014). This complex network of physical processes is collectively known as 'feedback'.

Theoretically, modelling feedback represents a formidable challenge. This is because its ab initio implementation in cosmological simulations is hampered by the range of scales (from Mpc to sub-pc; Agertz et al. 2013) involved in the problem, and also by the complexity of the physical network. Nevertheless, some simple scalings with global properties of galaxies have provided at least a phenomenological link to observations (Davé, Finlator & Oppenheimer 2012; Dayal et al. 2014).

Observations provide crucial insights and guidance into outflow physics and driving. The most studied local starburst galaxy, M82, shows a prominent biconical, multiphase outflow.

X-ray observations suggest the coexistence of hot ($\sim 10^7$ K) gas together with a warm ($\sim 10^3$ K) Hα-emitting phase (Lehnert, Heckman & Weaver 1999) in which cold (~ 10 K), molecular clumps are embedded, as revealed by CO observations (Walter, Weiss & Scoville 2002). Evidence of outflows from local dwarf galaxies are also abundant (e.g. Martin, Kobulnicky & Heckman 2002; see also the review by Veilleux, Cecil & Bland-Hawthorn 2005). Finally, very fast (up to 1000–2000 km s^{-1}) AGN-driven outflows of molecular gas, extending on kpc scales, have been found in a dozen dusty star-forming galaxies (Veilleux et al. 2013; Cicone et al. 2014; Feruglio et al. 2015).

At higher redshifts, detecting outflows becomes much more difficult. However, thanks mostly to absorption line spectroscopy, the presence of powerful outflows in galaxies close to the peak of the cosmic star formation ($z \approx 2$–3), has been firmly assessed (Shapley et al. 2003; Steidel et al. 2010; Kacprzak et al. 2014; Rubin et al. 2014; Heckman et al. 2015; Schroetter et al. 2015). Pushing observations into the Epoch of Reionization (EoR, $z > 6$) is clearly the next frontier. This would be particularly important for several reasons. First, quasar absorption line experiments have shown that the IGM is already substantially enriched by the end of the EoR (D'Odorico et al. 2013), thus bringing a strong argument in favour of widespread galactic outflow activity. Secondly, a consensus exists that reionization has been primarily driven by ionizing photons produced by low-mass galaxies (Choudhury & Ferrara 2007; Choudhury, Ferrara & Gallerani 2008; Finkelstein et al. 2012; Mitra, Choudhury & Ferrara 2012; Bouwens et al. 2015; Mitra, Choudhury & Ferrara 2015; Robertson et al. 2015) which are the most sensitive to feedback effects. Thus, outflows have likely regulated the reionization process both by modulating star formation and the escape of LyC photons through the resulting hot cavities.

Encouraged by the success in detecting outflows from high-z quasars using sub-mm lines (Maiolino et al. 2012; Cicone et al. 2015), in this paper we present the first attempt to use Atacama Large Millimeter Array (ALMA) data to detect outflows from the analysis of the [C ii] 158 µm line emitted by galaxies in the EoR.

2 ALMA OBSERVATIONS

We consider a sample of high-z ($5.2 \lesssim z \lesssim 5.7$) galaxies for which spectra of the [C ii]158 µm line have been obtained with ALMA at an angular resolution of[1] ~ 0.6 arcsec by Capak et al. (2015, hereafter C15). We consider HZ8 and its 'companion' galaxy HZ8W as two distinct sources. We do not consider the quasar HZ5, and the galaxy HZ10 since its [C ii] emission line is located at the edge of the observed spectrum. The final sample consists of nine star-forming galaxies ($5 \lesssim$ SFR $\lesssim 70\,M_\odot\,yr^{-1}$) characterized by a stellar masses $\sim 10^{10}\,M_\odot$.

The Common Astronomy Software Application (CASA) was used for data reduction and analysis. The continuum subtraction was done by creating a continuum image from the three line-free ~ 2 GHz base-bands, and then subtracting a model thereof in the visibility plane. A linear subtraction (i.e. zeroth-order polynomial) was performed across the bandpass. We underline that the galaxies of the

C15 sample exhibit a systematically low dust content: only three out of the nine sources considered (namely HZ4, HZ6 and HZ9) have been detected in continuum emission with fluxes ~ 0.1–0.5 mJy. A Briggs flexible weighting scheme (Robust = 1) was adopted.[2] For what concerns the bandpass calibration, the shape in each band was measured on a calibrator, to divide out the instrumental response.[3] We have removed from the observed spectra those pixels where the atmospheric transmission shows enhanced dips at the relevant frequencies, assuming $pwv = 2$ mm for the precipitable water vapour. This is a conservative assumption, since the actual values for these observations were $pwv = 0.2$–1.9 mm (mostly < 1 mm). Pixels removal has been necessary only for HZ6 (see the grey shaded region in Fig. 1).

3 METHOD

Although [C ii] emission is clearly detected ($\geq 6\sigma$) in all the galaxies considered, the quality of their spectra is not sufficient for a detailed analysis of the [C ii] line profile in individual galaxies. To overcome this difficulty, we adopt an inferential statistical approach. First of all, we start from the *null hypothesis* that the [C ii] lines of our sample are well described by a Gaussian profile.

For each galaxy in the C15 sample, we fit the [C ii] emission line (F_{obs}) with a Gaussian function (F_{mod}), whose free parameters are the full width at half-maximum (FWHM), the peak flux (F_{peak}), and the centre velocity, (v_0). Moreover, we quantify the noise (σ_n) of the spectrum by computing the standard deviation of the observed flux in pixels characterized by a velocity $|v| > v_{cont}$, where[4] $v_{cont} = 700$ km s^{-1}. We find $0.3 < \sigma_n/[\mathrm{mJy}] < 1.3$ with a mean value $\langle \sigma_n \rangle = 0.7$ mJy. Finally, we compute the residuals by subtracting the best-fitting model from the observed spectrum, and normalize them to the noise, $R = (F_{obs} - F_{mod})\sigma_n^{-1}$. As a sanity check of the method, for each galaxy, we also compute a *standard normal deviate*,[5] hereafter called G.

In Fig. 1, we show the results from the above procedure for each galaxy in the sample. In each panel, we plot the observed spectrum (yellow shaded region), the Gaussian best fit (red line) and the normalized residual (yellow shaded region in the sub-panel). For each galaxy, we report in the figure the best-fitting values of the

---

[2] In the case of HZ6, we have applied a natural weighting scheme (Robust = 2) to the ALMA data. We have also tried to fit the [C ii] emission line extracted from a no continuum subtracted cube with a 'Gaussian + continuum' function. We have checked that different weighting schemes and/or continuum subtraction techniques do not affect the main result of this work.
[3] The sources J0538−4405, J0522−3627 and J1037−2934 were used for the bandpass calibration. From the ALMA calibrator source catalogue (https://almascience.eso.org/alma-data/calibrator-catalogue), it can be seen that these sources show flux variations of 50–65 per cent on a time-scale of 6 yr (i.e. < 0.03 per cent per day). Thus, uncertainties related to calibrators' variability are expected to be negligible. Moreover, we have checked that, within 1σ flux density uncertainties, the spectra of the bandpass calibrators are flat. Ganymede, Pallas and Callisto were used for the flux calibration (providing an accuracy of ~ 5 per cent); J1058+0133 and J1008+0621 for the phase calibration.
[4] The value of v_{cont} has been chosen in order to minimize the contamination by broad wings. However, its specific value does not affect the results of our study.
[5] A *standard normal deviate* is a random number extracted by a Gaussian distribution having mean equal to zero and standard deviation equal to one.
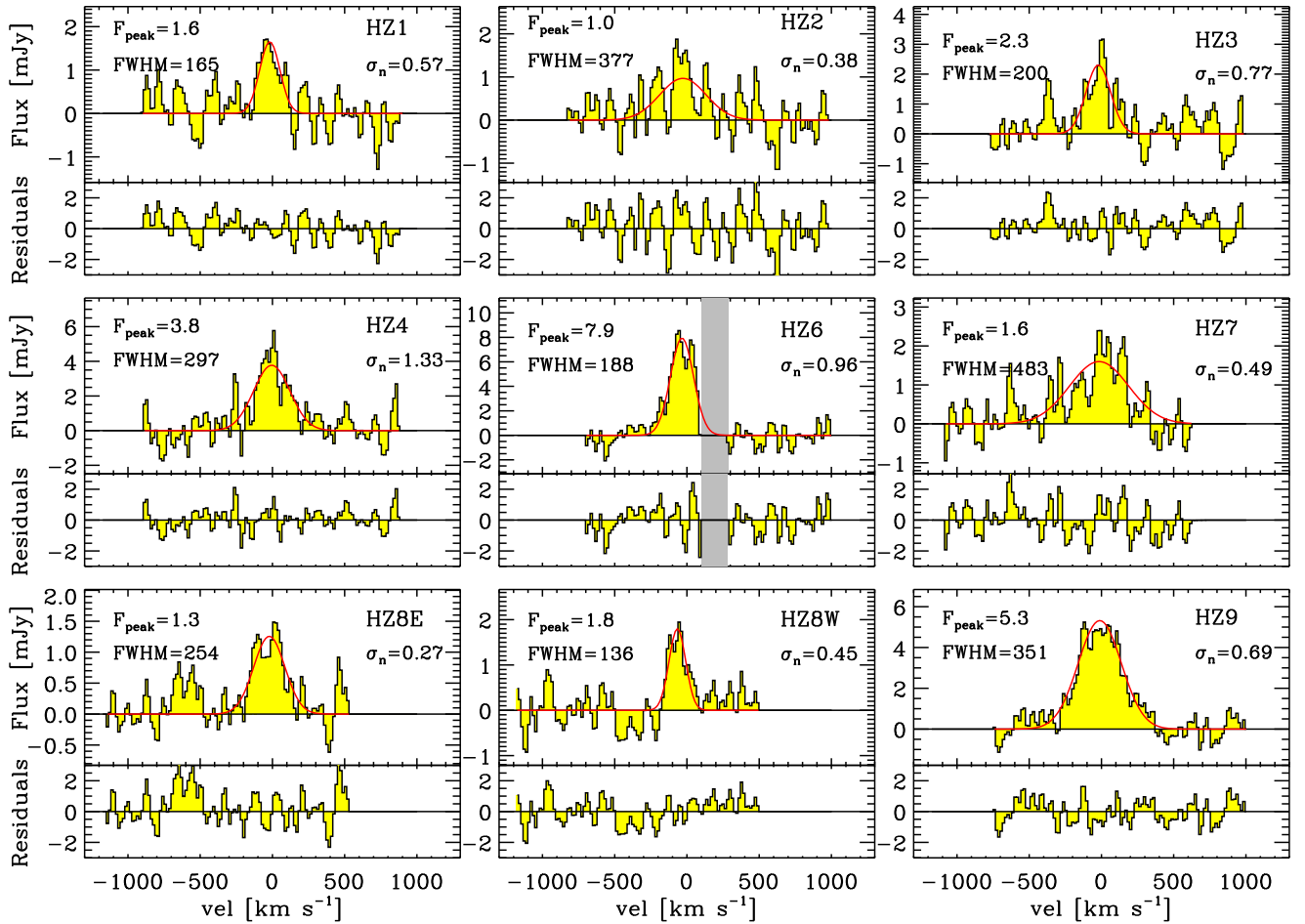
Figure 1. [C II] emission lines observed with ALMA by C15 (yellow shaded regions). The red solid lines represent the single Gaussian fit to the data. For each galaxy, the best-fitting parameters (FWHM, F_{peak}) and the noise (σ_n) are reported; the normalized residuals are shown in the bottom panels by the yellow shaded regions; the grey shaded region in HZ6 represents a frequency range in which the atmospheric transmission shows an enhanced dip in the case of $pwv = 2$ mm.

peak flux F_{peak}, the FWHM of the [C II] line, and σ_n. We thus combine both R and G of all galaxies into single arrays:

$$R^{tot}(v) = \frac{1}{n_{gal}} \Sigma_{j=1}^{n_{gal}} R^j(v); \; G^{tot}(v) = \frac{1}{n_{gal}} \Sigma_{j=1}^{n_{gal}} G^j(v). \quad (1)$$

The stacked signal, rebinned to 50 km s^{-1}, and multiplied for $\langle \sigma_n \rangle$ is shown in the left-hand panel of Fig. 2, where we have differentiated pixels characterized by $|v| > v_{cont}$ (blue shaded region), from those with $|v| < v_{cont}$ (magenta shaded region). For each spectral bin, on top of the spectrum, we report the number of galaxies contributing to the corresponding flux. In the same figure, we plot $G^{tot} \times \langle \sigma_n \rangle$ with a hatched grey region, rebinned to 50 km s^{-1}, and $R^{tot} \times \langle \sigma_n \rangle$ with a solid black line at a resolution of 20 km s^{-1}. We find a flux excess of ∼0.5 mJy extended over ∼1000 km s^{-1}.

We underline that the final stacked signal takes into account the differences between individual sources, since for each galaxy we subtracted the individual fit from the observed spectrum and normalized the residual to its own σ_n. Both in individual sources and in the stacked spectrum, the analysis takes into account the removal of a residual continuum term due to faint, individually undetected continuum or residuals in the subtraction.

If the observed spectra were completely determined by a single Gaussian [C II] emission line, the flux density of R^{tot} should consist simply of noise. In other words, both R^{tot} and G^{tot} should be

described, by construction, by a *standard normal deviate*. We compute the cumulative distribution function (CDF) both of R^{tot} and G^{tot}, at a resolution of 20 km s^{-1}, and we compare them with the error function:

$$\text{erf}(x) = \frac{2}{\sqrt{\pi}} \int_0^x e^{-t^2} dt, \quad (2)$$

that describes the CDF of a *standard normal deviate*.

The resulting CDFs of R^{tot} (solid black line) and G^{tot} (dashed black line) are shown in the right-hand panel of Fig. 2. The blue and magenta lines show the CDF of R^{tot} for $|v| > v_{cont}$ and $|v| < v_{cont}$, respectively, while the grey shaded region is the result of the CDFs computed for 500 *standard normal deviates*. Finally, the dotted line represents the CDF described by equation (2). While the CDF of R^{tot} strongly differs from the G^{tot} CDF (particularly for $|v| < v_{cont}$), the latter is, as expected, well within the grey shaded regions. This sanity check ensures that the method adopted does not artificially introduce any deviation from a *standard normal deviate*.

To quantify the deviation of the CDFs from the error function erf, we apply the Kolmogorov–Smirnov (KS) test to our data: we compute (i) the KS statistics, namely the maximum deviation (D_{KS}) of the observed CDFs from the erf and the (ii) the KS probability (P_{KS}); small values of the KS probability imply that a CDF is significantly different from the erf. We apply the KS test to the
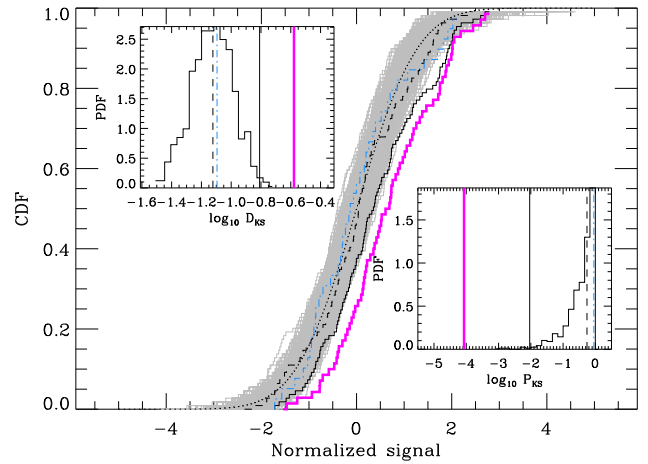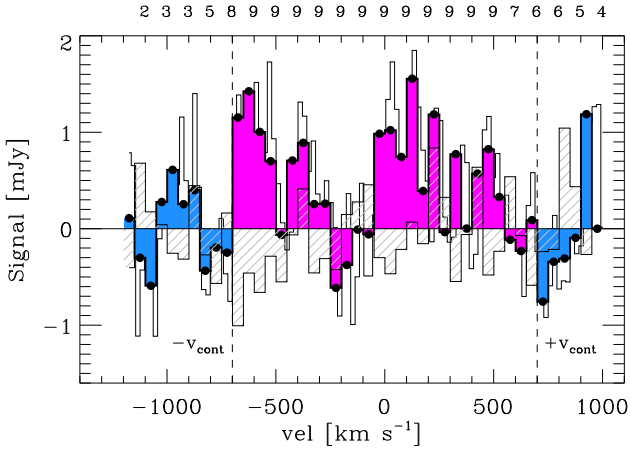
Figure 2. Left-hand panel: The coloured histogram shows $R^{tot} \times \langle \sigma_n \rangle$, i.e. the combined normalized residuals, multiplied for the mean value of the noise of all galaxies $\langle \sigma_n \rangle = 0.7$ mJy. The magenta region refers to pixels characterized by $|v| < v_{cont}$, where $v_{cont} = 700$ km s^{-1}, while the blue region represents the region used for the noise determination, namely $|v| > v_{cont}$. The grey hatched histogram represents G^{tot}, i.e. the combined standard normal deviates (see footnote 5). Both signals have been rebinned to 50 km s^{-1}. For each spectral bin we report, on the top of the spectrum, the number of galaxies that contribute to the corresponding flux. The thin solid black line shows $R^{tot} \times \langle \sigma_n \rangle$ at a resolution of 20 km s^{-1}. Right-hand panel: CDFs of R^{tot} (solid black line) and G^{tot} (dashed black line), rebinned to a spectral resolution of 20 km s^{-1}. The solid thick magenta (dot–dashed blue) line shows the CDF of R^{tot} computed in the velocity range $|v| < v_{cont}$ ($|v| > v_{cont}$). The grey shaded region represents the CDFs of 500 standard normal deviates, while the dotted line denotes the error function. See the main text for a description of the insets.

Table 1. Results for the Kolmogorov–Smirnov (KS) and Anderson–Darling (AD) tests.

	KS probability	KS statistics	AD statistics
G^{tot}	0.55	0.07	0.01
R^{tot}	4×10^{-3}	0.17	0.12
R^{tot} ($|v| < v_{cont}$)	3×10^{-5}	0.28	0.31
R^{tot} ($|v| > v_{cont}$)	0.90	0.08	0.02

Table 2. Parameter ranges for Monte Carlo simulations of synthetic profiles.

	Outflow	Satellites	Rotating disc
F_{Peak}^{narrow} (mJy)	1–7	–	–
σ^{narrow} (km s^{-1})	60–160	–	–
F_{Peak}^{broad} (mJy)	0.3–0.6	–	–
σ^{broad} (km s^{-1})	100–500	–	–
# satellites	–	1	–
F_{Peak}^{sat} (mJy)	–	0.1–0.4	–
σ^{sat} (km s^{-1})	–	20–50	–
F_{Peak}^{RD} (mJy)	–	–	1–7
v_c (km s^{-1})	–	–	50–200
σ_{gas} (km s^{-1})	–	–	8–50

CDF of G^{tot} and R^{tot} and we report the results in Table 1. Moreover, we quantify the deviation of the CDFs of the random Gaussian deviates G_i from the error function erf. In the bottom-right and top-left insets of Fig. 2 (right-hand panel), we show the probability distribution function (PDF) of $D_{KS}^{G_i}$ and $P_{KS}^{G_i}$, respectively, along with the results shown in Table 1. The residual flux clearly exceeds that of a *standard normal deviates*. This result is also confirmed by applying the Anderson–Darling (AD) test to the data. According to this test, a sample is significantly different from a random Gaussian deviate if the AD statistics is larger than 0.05 (see the third column in Table 1).

4 INTERPRETING THE FLUX EXCESS

The reported flux excess leads us to reject the *null hypothesis* that a Gaussian model accurately describes the [C II] line profiles observed in the C15 sample. Thus, the next step is to look for *alternative hypothesis* that better describes the [C II] line shape of these high-z galaxies. Several effects can explain the deviation of an emission line from a Gaussian profile:

(i) If SN-driven outflows are present as predicted (e.g. Pallottini et al. 2017, see also Section 5), broad wings superposed to a narrower Gaussian core should feature the [C II] line profile.

(ii) A multipeaked profile might result from the collective emission of satellite galaxies (e.g. Vallini et al. 2013, 2015).

(iii) If a rotating disc is present, the line profile might take a double-horned profile (e.g. de Blok & Walter 2014).

To analyse these possibilities, we produce three sets of 500 Monte Carlo simulations of [C II] emission lines with different profiles, depending on the scenario considered (see Sections 4.1, 4.2, 4.3 below). To simulate the observed noise, we add to each synthetic spectrum a Gaussian deviate with zero mean and $0.3 < \sigma_n/[\text{mJy}] < 1.3$. For each scenario, we divide the full synthetic sample into subsamples of nine galaxies, and we apply to each sub-sample the same method as described in Section 3: we first fit each synthetic profile with a single Gaussian (presented in Fig. 4 in the next section); then, we normalize the residual to σ_n; finally, we stack the nine simulated residuals into a single signal and we multiply it for $\langle \sigma_n \rangle$ (presented in Fig. 5 in the next section).

4.1 Outflow

In this first scenario, synthetic [C II] emission lines are constituted by the sum of a narrow Gaussian (defined by its peak flux F_{peak}^{narrow} and RMS σ^{narrow}) plus a broad Gaussian profile (F_{peak}^{broad}; σ^{broad}). We consider the parameter ranges shown in Table 2. We assume the
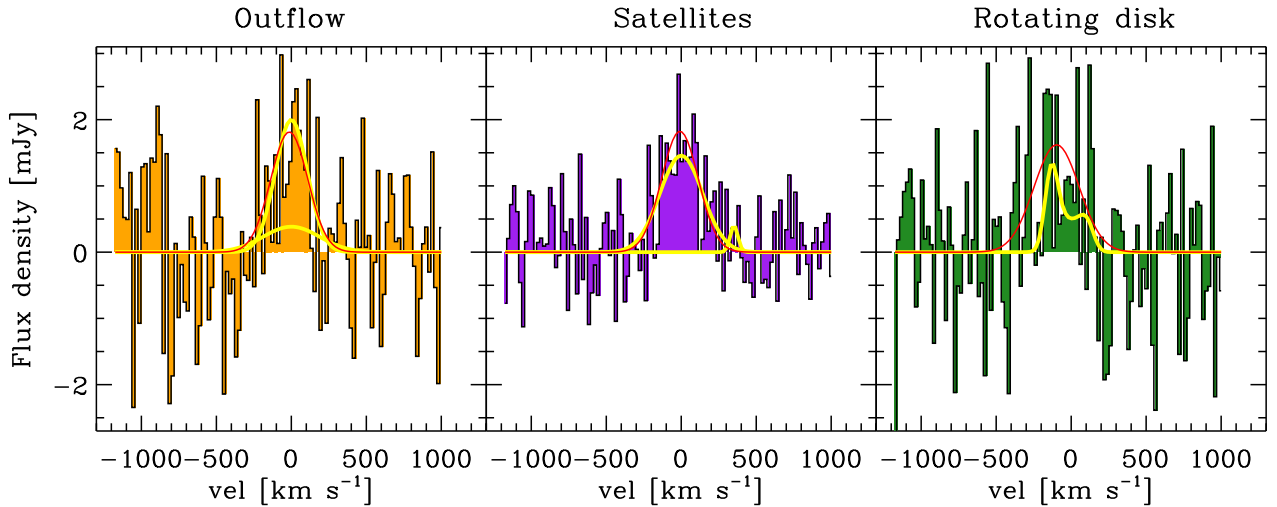
Figure 3. Examples of synthetic spectra for the outflow (left-hand panel), satellites (middle panel) and rotating disc (right-hand panel) scenarios. The thick yellow lines represent the original synthetic spectra, while coloured shaded regions show the final spectra, after adding noise. The solid red lines represent the best-fitting single Gaussian profile.

same central velocity both for the narrow and broad components. We take σ^{broad} by numerical simulation results (see Section 5).

4.2 Satellites

To mimic the effect of satellites on the [C II] line profiles, we consider the sum of a Gaussian profile (defined by $F_{\mathrm{peak}}^{\mathrm{narrow}}$ and σ^{narrow}) plus a number N_{sat} of Gaussians characterized by $F_{\mathrm{peak}}^{\mathrm{sat}}$ and σ^{sat} (see Table 2). To constrain σ^{sat}, we consider, as upper limit, the minimum value of σ in the C15 sample ($\sigma = 50 \, \mathrm{km \, s^{-1}}$), and, as lower limit, the minimum value of σ found in all the [C II] emission lines detected so far at high redshift ($\sigma = 20 \, \mathrm{km \, s^{-1}}$; Pentericci et al. 2016). For what concerns $F_{\mathrm{peak}}^{\mathrm{sat}}$, we use the M_{UV}–F_{peak} relation presented in Pallottini et al. (2015, see their equation 2). The UV magnitude limit of the C15 sample ($M_{\mathrm{UV}} > -19.94$) converts into an upper limit for the [C II] emission line peak ($F_{\mathrm{peak}}^{\mathrm{sat}} < 0.4 \, \mathrm{mJy}$; see also Vallini et al. 2015; Yue et al. 2015). We note that this UV magnitude roughly corresponds to satellites with $\mathrm{SFR}^{\mathrm{sat}} \sim 1 \, \mathrm{M_\odot \, yr^{-1}}$ and $M_*^{\mathrm{sat}} \sim 10^9 \, \mathrm{M_\odot}$. Finally, to compute the number of satellites that we expect to surround the galaxies of our sample, we adopt the halo occupation distribution model (see equation 14 by Yue et al. 2013). The C15 sample consists of $M_* \sim 10^{10} \, \mathrm{M_\odot}$ galaxies that are expected to be hosted in $M_{\mathrm{DM}} = 6 \times 10^{11} \, \mathrm{M_\odot}$ dark matter (DM) halo. In such halo, we expect to find ∼4 satellites with $M_*^{\mathrm{sat}} \sim 10^9 \, \mathrm{M_\odot}$. Given that these satellites can be located at a distance up to $r_{\mathrm{vir}} \sim 40 \, \mathrm{kpc}$, we find that it is very unlikely to find any of them within 1–2 beams (∼3–7 kpc) of the ALMA observations. In our calculations, we use $F_{\mathrm{peak}}^{\mathrm{sat}} = 0.1$–$0.4 \, \mathrm{mJy}$ and we assume that, for each of the C15 galaxies, the ALMA beam encloses a number of satellites $N_{\mathrm{sat}} = 1$ (see Table 2). Thus, the contribution of satellites to the observed flux excess that we compute must be considered as a solid upper limit.

4.3 Rotating disc

To simulate the double-horned profile resulting from a rotating disc we refer to the work done by de Blok & Walter (2014, in particular see equation 1). A double-horned profile is specified by its peak flux $F_{\mathrm{peak}}^{\mathrm{RD}}$, the disc circular velocity v_{c} and the gas velocity dispersion σ_{gas}; the double horned is given by the convolution of a Gaussian

($F_{\mathrm{peak}}^{\mathrm{RD}}$, σ_{gas}) with the velocity profile $\psi(v) = (v^2 - v_{\mathrm{c}}^2)^{-1/2} \Theta(|v_{\mathrm{c}}| - v)/\pi$, where Θ is the Heaviside function. We consider the parameter ranges shown in Table 2.

4.4 Results

In Fig. 3, we show one example of synthetic emission line for each scenario described above (*outflow* in the left, *satellites* in the middle and *rotating disc* in the right-hand panel).

We model each synthetic spectrum with a single Gaussian profile: in Fig. 4, we show the PDF of the best-fitting Gaussian peak (left-hand panel) and σ (right-hand panel) (orange line for the *outflow*, violet line for the *satellites*, green line for the *rotating disc* scenarios). As a reference, we plot the min, the first quartile, the mean, the third quartile, and the maximum values resulting from the best-fitting models of the C15 sample. The nice agreement between the observed values and the synthetic ones shows that the simulated lines have properties consistent with data.

We calculate the residuals using the best-fitting Gaussians: in Fig. 5 (left/middle/right panels), we compare the observed flux excess (filled circles) with the one we obtain by applying our method to the simulated samples (*outflow/satellites/rotating disc*). The black thick lines represent the realizations that provide the best agreement with data, while the coloured shaded regions quantify the 1σ dispersion over the 500 realizations. This figure shows that our method, in the case of the *outflow* scenario, provides residuals that are in a qualitative better agreement with observations with respect to the *satellites* and *rotating disc* scenarios considered.

To be more quantitative, in Fig. 6, we compare the observed CDF (filled circles) with the ones extracted from synthetic samples (orange solid line for the *outflow*, violet dotted line for the *satellites*, green dashed line for the *rotating disc* scenarios). We apply the KS test between the observed and simulated CDFs and we report the results in Fig. 6. We find that the distance from the observed CDF is minimized by the *outflow* scenario ($D_{\mathrm{KS}} = 0.05$). In this case, the probability that the simulated CDF reproduces the observed one is maximum ($P_{\mathrm{KS}} = 1.0$). However, we cannot exclude that part of the flux excess we detect is due to emission from satellite galaxies. In fact, in the *satellites* scenario we find $D_{\mathrm{KS}} = 0.10$ and $P_{\mathrm{KS}} = 0.6$.
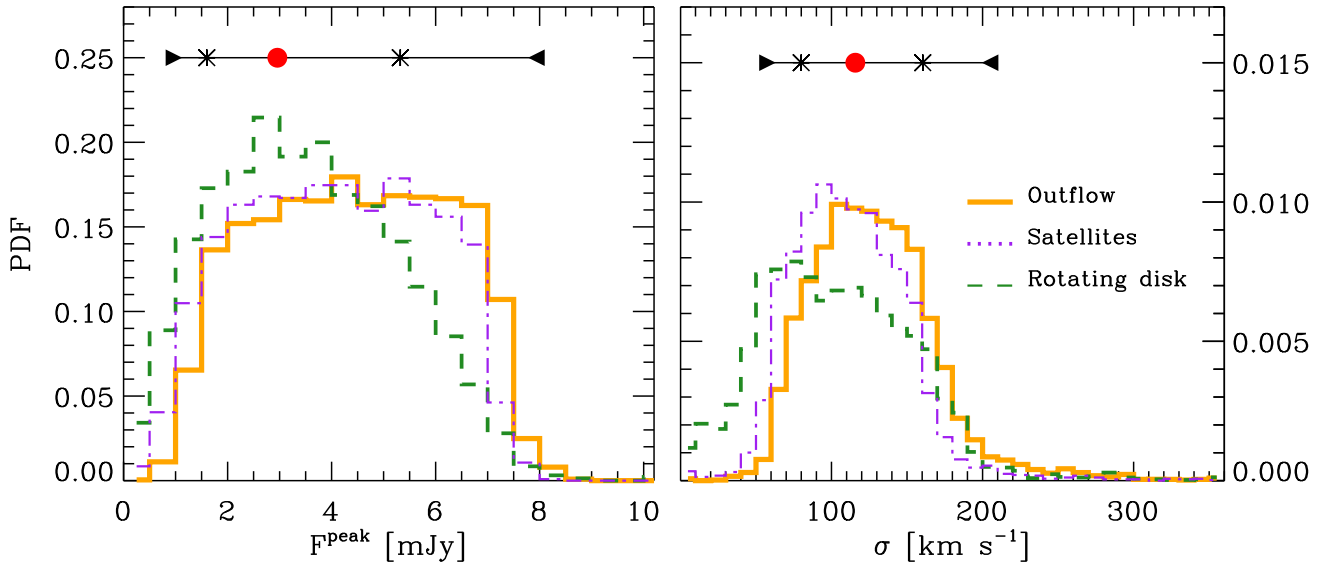
Figure 4. PDFsof the flux peak (F^{peak}, left-hand panel) and width (σ, right-hand panel) of the single Gaussian component that provides the best fit of the synthetic spectra for the models analysed. We plot the PDF for the outflow, satellites and rotating disc scenarios with a solid orange, dotted green and dashed violet line, respectively. As a reference, for both F^{peak} and σ we plot the min/first quartile/mean/third quartile/max values obtained from the best fit of the C15 sample with right triangle/asterisk/red circle/asterisk/left triangle, respectively.
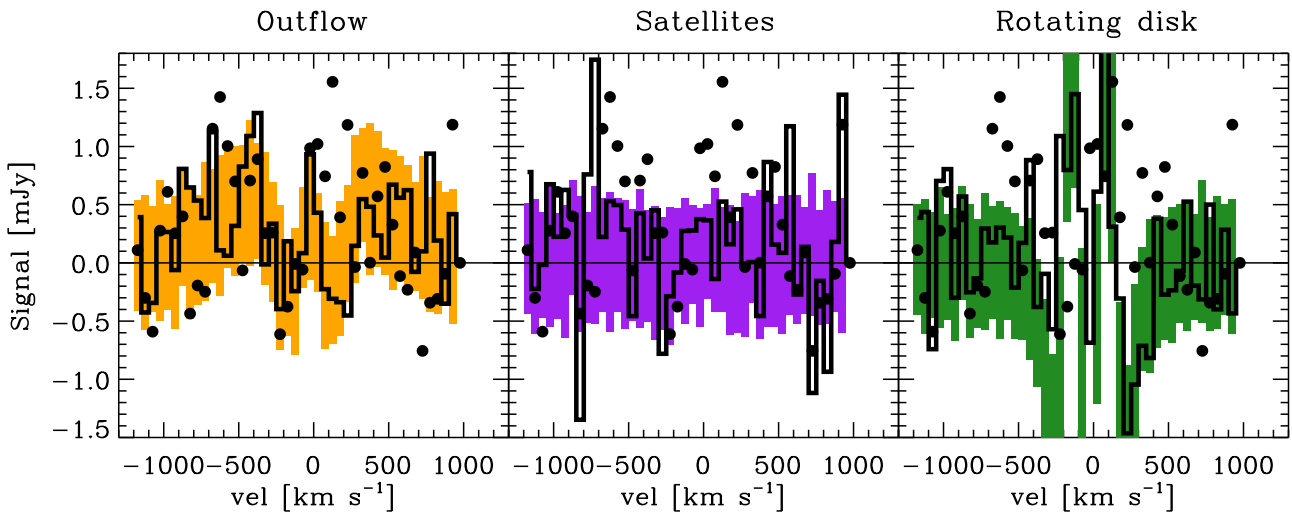

Figure 5. Combined residuals for the synthetic samples (see the left-hand panel of Fig. 2). Filled black circles refer to the C15 sample. The black thick lines represent the realizations that provide the best agreement with data, while the coloured shaded regions quantify the 1σ dispersion over the 500 realizations.

The *rotating disc* scenario is instead more difficult to be reconciled with observations: $D_{KS} = 0.13$, $P_{KS} = 0.3$.

This analysis suggests that the observed flux excess can be ascribed to broad wings of the [C II] line tracing a starburst-driven outflow. In the realization that better describes the observed flux excess, the average value of the flux peak broad component is $\langle F^{broad}_{peak} \rangle = 0.4 \pm 0.1$ mJy, while $\langle \sigma^{broad} \rangle = 360 \pm 140$ km s^{-1}, for a total [C II] luminosity $L^{broad}_{[C\ II]} = 2.9 \pm 1.2 \times 10^8$ L$_\odot$.

As a final test, we have divided our sample in two sub-samples: S1 containing HZ1, HZ2, HZ3 and HZ7, HZ8 and HZ8W, i.e. galaxies with SFR < 50 M$_\odot$ yr^{-1}, and S2 constituted by HZ4, HZ6 and HZ9, i.e. galaxies with SFR $\gtrsim 50$ M$_\odot$ yr^{-1}. In both cases, the deviation from a standard normal deviate is found, though the flux excess is stronger in the S2 sub-sample. This is expected as in the S2 sub-sample galaxies have more SNe available to drive outflows. However, the statistical significance

of this result is limited by the small number of galaxies in the sub-samples.

5 NUMERICAL SIMULATIONS

We test our results against zoomed hydrosimulations of high-redshift galaxies performed with the Adaptive Mesh Refinement (AMR) code RAMSES (Teyssier 2002). These simulations are fully described in Pallottini et al. (2017, hereafter P17); here, we summarize the aspects of the simulation that are relevant for this work.

Starting from cosmological initial conditions, we carry out a zoom-in simulation of a $z \sim 6$ DM halo of mass $\sim 10^{11}$ M$_\odot$ (virial radius of $\simeq 15$ kpc). In the zoomed-in region, the gas mass resolution is 10^4 M$_\odot$, and the AMR grid is refined to spatial scales $\simeq 30$ pc. We form stars from molecular hydrogen, following the model by Krumholz, McKee & Tumlinson (2009). Stellar feedback includes
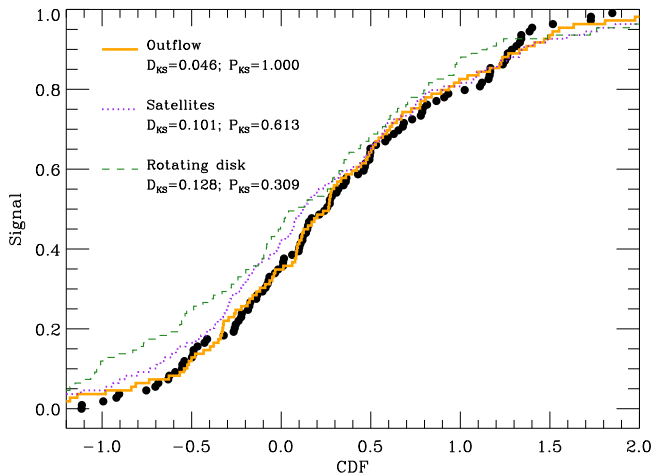
Figure 6. CDF of the residuals for the synthetic samples (see the right-hand panel of Fig. 2). Filled black circles refer to the CDF of C15 sample. Coloured lines represent the realizations that provide the best agreement with data. We also report the results of the KS test (KS statistics, D_{KS}, and KS probability, P_{KS}) between the observed CDF and the simulated ones.

SNe, winds from massive stars and radiation pressure (e.g. Agertz et al. 2013). We model the thermal and turbulent energy content of the gas according to the prescriptions by Agertz & Kravtsov (2015). We account for stellar energy inputs and yields that depend both on time and stellar populations (e.g. Kim et al. 2014).

At $z \sim 6$, the DM halo hosts a galaxy (named Dahlia) characterized by a stellar mass $M_* \sim 10^{10} M_\odot$ and an SFR $\sim 100 M_\odot yr^{-1}$. In the top panels of Fig. 7, we show a slice of the density and metallicity fields (left and right, respectively) along with the velocity field orthogonal to the line of sight. Within a radial distance $r \lesssim 5 \, kpc$ from Dahlia's centre, the gas has an average density of $n \simeq 10 \, cm^{-3}$, it is enriched to $Z \simeq 10^{-1} Z_\odot$, and rotates with a velocity $v_c \sim 100 \, km \, s^{-1}$. At $5 \lesssim (r/kpc) \lesssim 15$, Dahlia is surrounded by a bubble of low density ($n \simeq 10^{-1} \, cm^{-3}$), low metallicity ($Z \simeq 10^{-2} Z_\odot$) gas, outflowing at a speed $v \sim 100 \, km \, s^{-1}$. In the same region, dense ($n \simeq 1 \, cm^{-3}$) and almost metal free $Z \simeq 10^{-3} Z_\odot$ filaments are infalling with a velocity $v \sim 100 \, km \, s^{-1}$. These filaments penetrate Dahlia's circumgalactic medium at a distance of ∼7 kpc (half of the virial radius), mixing with such component and becoming progressively more isotropic. The effect of the rapidly decreasing density and metallicity with the distance from the central of the galaxy is that negligible [C II] emission is expected on scales $\gtrsim 3 \, kpc$ (see fig. 10 and equation 8 in P17).

To better quantify our analysis, we compute the mass flow rate[6] ($\dot{M}$) and the PDF of the radial velocity (v_r) at distances[7] $r \simeq 0.1, 2$ and 15 kpc. The results are shown in Fig. 7, in the bottom left and right panels, respectively. At the centre ($r \simeq 0.1 \, kpc$), we find high radial velocities ($\sim 500 \, km s^{-1}$) for both the infall and outflow.[8] As the infall fuels gas directly at the centre, Dahlia's SFR is mostly

---

[6] The mass flow rate at a distance r is defined as the material crossing a sphere of radius r: $\dot{M} = \int \rho v \cdot dA$, where dA is the surface area element, $\rho = \mu m_p n$ is the proton mass and $v_r < 0$ for infalling gas and $v_r > 0$ for outflowing gas.

[7] To compute the radial velocity PDF, we consider spherical shells with a thickness $\simeq 100 \, pc$ centred at a distance r from Dahlia. This ensures that for each shell the PDF contains a minimum of ∼100 resolution elements.

[8] We use these values of radial velocity to model the σ^{broad} in the *outflow* scenario presented in Section 4.1.

concentrated around $r \simeq 0.1 \, kpc$. Via stellar feedback, this in turn causes high outflow velocities. Within $r \simeq 2 \, kpc$, the mass inflow and the outflow rate are nearly equal ($\sim 30 M_\odot yr^{-1}$). Interestingly, the two rates are roughly equal also for metals. We interpret this as a result of efficient turbulent mixing between the two flows. For $r \gtrsim 2 \, kpc$, the velocity depends only mildly on radius, and since the density is approximately $\rho \propto r^{-2}$, the observed constancy of the outflow rate is mostly a consequence of a geometrical effect. At $r \gtrsim 5 \, kpc$, the infall rate drops by a factor of $\gtrsim 10$ below the outflow rate. This is caused by the different spatial structure of the two flows: while the incoming gas rains on to Dahlia along narrow filaments, the outflow is essentially spherically symmetric. Note that the outflow is ∼10 times more enriched than the infall, as most of the gas is essentially of pristine composition; thus, we expect the infall contribution to [C II] emission to be negligible with respect to the outflow. The ratio mildly declines with radius because of the progressive dilution of the outflow metal content with the IGM. The presence of peaks at $r \sim 12$ and $20 \, kpc$ is due to the presence of satellite galaxies. As projection effects are in place, we underline that it is quite unlikely to find such satellites in the ∼3 kpc beam centred on the main galaxy (Dahlia in this case) from which the [C II] spectra are calculated in C15. From fig. 10 by P17, we note that few (∼3) molecular clouds of mass $\sim 10^6 M_\odot$ are present within $\lesssim 5 \, kpc$ from the centre of Dahlia; however, such clumps negligibly contribute to the [C II] emission since their typical luminosity is $L_{C II}/L_\odot \simeq 10^5$ (see equation 8 in P17), i.e. a factor of $\sim 10^3$ less than the main galaxy.

6 CONCLUSIONS

We have analysed the [C II] emission lines obtained with ALMA (C15) in a sample of nine star-forming ($5 \lesssim SFR \lesssim 70 M_\odot yr^{-1}$) high-$z$ ($5.2 \lesssim z \lesssim 5.7$) galaxies. We have fitted each [C II] emission line with a Gaussian function and we have computed the residual by subtracting the best-fitting model from the data. By combining the residuals of all the galaxies, we have found a flux excess that can be ascribed to broad wings of the [C II] line tracing a starburst-driven outflow. In order to get a rough estimate of the outflow rate $\dot{M}$, we use the following equation:

$$\dot{M} = v_{outfl} \frac{M_{outfl}}{R_{outfl}}, \qquad (3)$$

where $v_{outfl} \sim 500 \, km \, s^{-1}$ is given by the largest velocity at which we observed the flux excess (see the left-hand panel of Fig. 2), and $M_{outfl} = 2.1 \pm 0.9 \times 10^8 M_\odot$ is the total mass of the outflowing gas, obtained as in Maiolino et al. (2012, see their equation 1) considering the [C II] luminosity of the broad component estimated in Section 4.4. For what concerns R_{outfl}, we assume that the spatial extent of the outflow is of the order of the radius of the deconvolved [C II] emission sizes, i.e. ∼1.9 kpc, a value consistent with the half-light radii of $z \sim 6$ LAEs (Taniguchi et al. 2009; Malhotra et al. 2011; Shibuya, Ouchi & Harikane 2015). Through this procedure, we infer an outflow rate of $\dot{M} = 54 \pm 23 M_\odot yr^{-1}$. Given that the star formation rate of our sample is SFR $= 31 \pm 20 M_\odot yr^{-1}$, we estimate a loading factor $\eta = \dot{M}/SFR = 1.7 \pm 1.3$, in nice agreement with the results found in local starbursts (see the top-left panel of fig. 6 by Heckman et al. 2015).

Moreover, Heckman & Borthakur (2016) have recently analysed a sample of low-z ($0.2 \lesssim z \lesssim 0.7$) galaxies characterized by a large range of SFRs ($10^{-2} \lesssim SFR/[M_\odot \, yr^{-1}] \lesssim 10^3$), and found a strong correlation between the specific SFR (sSFR $=$ SFR/M_*) and v_{max} (see the bottom-left panel of their fig. 1). From their scaling relation,
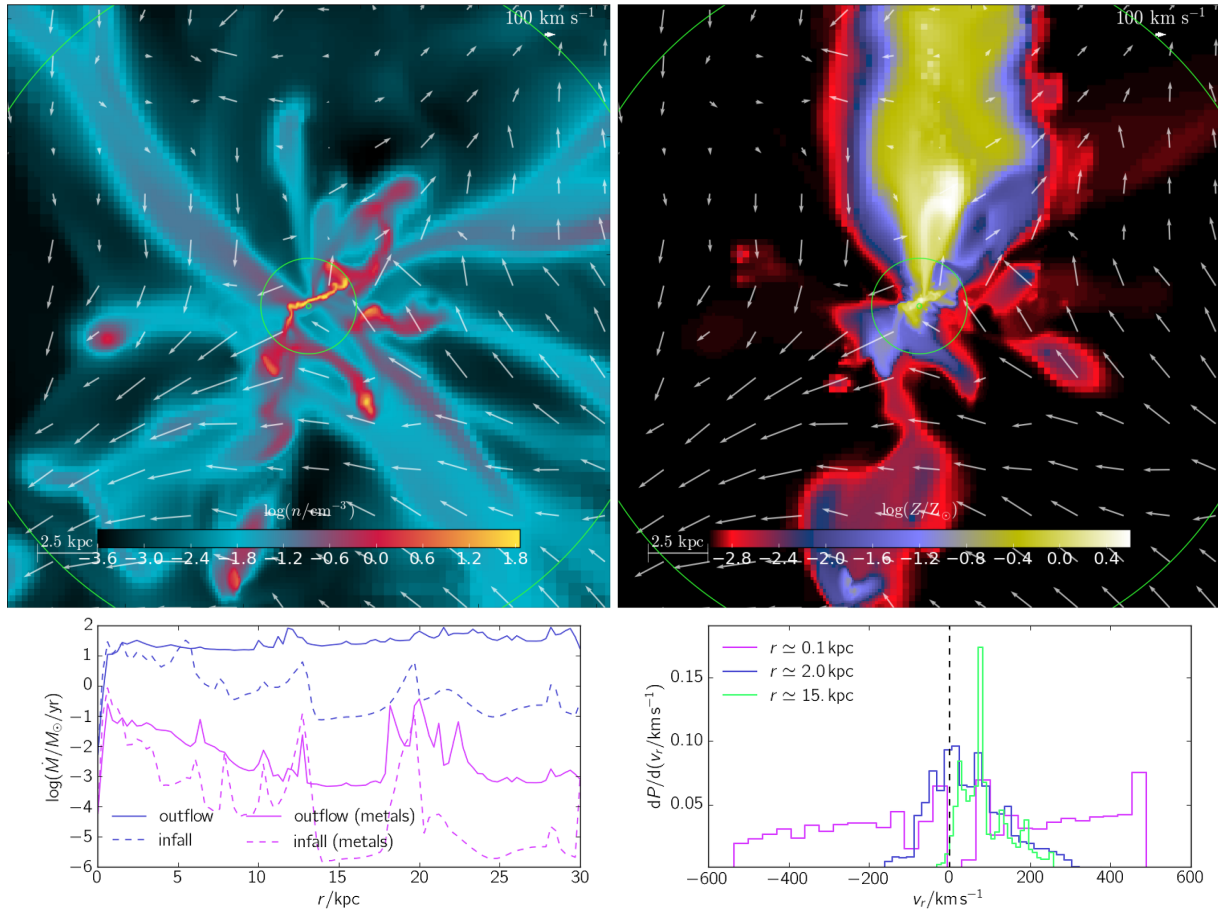
Figure 7. Slice of the density (n/cm^{-3}, upper-left panel) and metallicity ($Z/Z_\odot$, upper-right panel) fields centred on the simulated galaxy Dahlia. In both maps, the velocity field orthogonal to the line of sight is overplotted with white arrows and the spatial scale is indicated in the lower-left corner. Green circles indicate a distance of $r/kpc \simeq 0.1, 2, 15$ from the centre. The lower-left panel shows the radially averaged outflow (solid line) and infall (dashed line) rate profiles for the gas (blue) and metals (magenta). The lower-right panel shows the PDF of the radial velocity (v_r) calculated for the gas at distance $r \simeq 0.1$ kpc (magenta), $r \simeq 2$ kpc (blue), $r \simeq 15$ kpc (green).

we expect $v_{max} \sim 500$ km s^{-1} for an sSFR $\sim 3 \times 10^{-9}$yr^{-1}, that is once more consistent with our findings.

We further note that one galaxy of the sample used in this work, namely HZ1, also shows strong Ly α emission ($L_{Ly\alpha} \sim 1.5 \times 10^8$ L$_\odot$; Mallery et al. 2012, note that in their paper HZ1 is called N8bb-54-1862). The Ly α line has an equivalent width EW$_{Ly\alpha} \sim 5$ Å and results to be redshifted with respect to the [C II] line by ~ 160 km s^{-1}, a value that is consistent with those reported for galaxies with similar UV luminosities and Ly α EWs (Erb et al. 2014; see also Willott et al. 2015; Pentericci et al. 2016; Carniani et al. 2017). Although the velocity offset between the Ly α line and the systemic redshift of galaxies could be ascribed to the presence of outflowing gas, it is important to underline that the Ly α line profile is affected by absorption from neutral hydrogen in the IGM and by absorption/scattering from dust in the ISM (e.g. Verhamme, Schaerer & Maselli 2006). Vice versa, both processes do not affect the [C II] line profile. Thus, the origin of the velocity offset between the Ly α and [C II] lines is still argument of debate.

We test the results of our analysis against state-of-the-art hydrodynamical simulations of Dahlia (P17), a star forming (SFR ~ 100 M$_\odot$yr^{-1}) $z \sim 6$ galaxy. Star formation in the simulations is regulated by stellar feedback as radiation pressure and stellar winds from massive stars, and SNe explosions. We find that, at a distance $r \lesssim 5$ kpc from the Dahlia centre, the infall rate is balanced

by outflowing gas with $\dot{M} \sim 30$ M$_\odot$ yr^{-1}. At larger distances, the outflow rate remains almost constant, while infalls are characterized by $\dot{M} \sim 1$ M$_\odot$ yr^{-1}. We underline that we cannot resolve [C II] emission arising from scales smaller than the ALMA beam (~ 3–4 kpc). Thus, the observed [C II] emission collects the contribution from all the material within this distance. Our simulations suggest that the flux excess resulting from our analysis at large velocities (~ 500 km s^{-1}) mostly arises from gas located at small distance from the centre of the galaxy (~ 0.1 kpc), while slower moving gas (still with velocities up to ~ 100 km s^{-1}) can be found at larger distances ($\gtrsim 2$ kpc).

The simulation outcomes support our interpretation of the ALMA data suggesting that starburst-driven outflows are in place in the EoR. However, we warn here that we are comparing an observed signal stacked from nine galaxies with a single synthetic galaxy. For a more specific comparison, we urge to get deeper observations of the [C II] line in the galaxies of this sample to better characterize stellar feedback at high-z and to understand its role in shaping early galaxy formation.

It would be interesting to apply the stacked analysis discussed in this work to other samples of galaxies and/or to extend the sample considered here. Other [C II] emitting galaxies (~ 14) have been indeed discovered at high-z in the last few years (e.g. Maiolino et al. 2015; Willott et al. 2015; Aravena et al. 2016;

Knudsen et al. 2016; Pentericci et al. 2016; Bradač et al. 2017; see also table 3 in Olsen et al. 2017 for an updated list of [C II] observations in $z \gtrsim 5$ star-forming galaxies). However, these observations span a large range in terms of redshift ($6 < z < 8$) and SFR (from few to almost thousands $M_\odot$ yr^{-1}). Thus, to date, the C15 sample represents the largest, homogeneous sample available for this kind of study.

ACKNOWLEDGEMENTS

REFERENCES

Agertz O., Kravtsov A. V., 2015, ApJ, 804, 18
Agertz O., Kravtsov A. V., Leitner S. N., Gnedin N. Y., 2013, ApJ, 770, 25
Aravena M. et al., 2016, ApJ, 833, 71
Bouwens R. J. et al., 2014, ApJ, 793, 115
Bouwens R. J., Illingworth G. D., Oesch P. A., Caruana J., Holwerda B., Smit R., Wilkins S., 2015, ApJ, 811, 140
Bradač M. et al., 2017, ApJ, 836, L2
Capak P. L. et al., 2015, Nature, 522, 455 (C15)
Carniani S. et al., 2017, A&A, 605, A42
Choudhury T. R., Ferrara A., 2007, MNRAS, 380, L6
Choudhury T. R., Ferrara A., Gallerani S., 2008, MNRAS, 385, L58
Cicone C. et al., 2014, A&A, 562, A21
Cicone C. et al., 2015, A&A, 574, A14
D'Odorico V. et al., 2013, MNRAS, 435, 1198
Davé R., Finlator K., Oppenheimer B. D., 2012, MNRAS, 421, 98
Dayal P., Ferrara A., Dunlop J. S., Pacucci F., 2014, MNRAS, 445, 2545
de Blok W. J. G., Walter F., 2014, AJ, 147, 96
Dekel A., Silk J., 1986, ApJ, 303, 39
Dunlop J. S., 2013, in Wiklind T., Mobasher B., Bromm V., eds., Astrophysics and Space Science Library, Vol. 396, The First Galaxies. Springer-Verlag, Berlin, p. 223
Erb D. K. et al., 2014, ApJ, 795, 33
Feruglio C. et al., 2015, A&A, 583, A99
Finkelstein S. L. et al., 2012, ApJ, 758, 93
Heckman T. M., Borthakur S., 2016, ApJ, 822, 9
Heckman T. M., Alexandroff R. M., Borthakur S., Overzier R., Leitherer C., 2015, ApJ, 809, 147
Hopkins P. F., Quataert E., Murray N., 2012, MNRAS, 421, 3522
Kacprzak G. G. et al., 2014, ApJ, 792, L12
Kim J.-h. et al., 2014, ApJS, 210, 14
Knudsen K. K., Richard J., Kneib J.-P., Jauzac M., Clément B., Drouart G., Egami E., Lindroos L., 2016, MNRAS, 462, L6
Krumholz M. R., McKee C. F., Tumlinson J., 2009, ApJ, 693, 216
Lehnert M. D., Heckman T. M., Weaver K. A., 1999, ApJ, 523, 575
Liang C. J., Kravtsov A. V., Agertz O., 2016, MNRAS, 458, 1164
Mac Low M.-M., Ferrara A., 1999, ApJ, 513, 142
Maiolino R. et al., 2012, MNRAS, 425, L66
Maiolino R. et al., 2015, MNRAS, 452, 54
Malhotra S., Rhoads J., Finkelstein S., Hathi N., Nilsson K., McLinden E., Pirzkal N., 2011, BAAS, 43, 407.03
Mallery R. P. et al., 2012, ApJ, 760, 128
Martin C. L., Kobulnicky H. A., Heckman T. M., 2002, ApJ, 574, 663
Mitra S., Choudhury T. R., Ferrara A., 2012, MNRAS, 419, 1480
Mitra S., Choudhury T. R., Ferrara A., 2015, MNRAS, 454, L76
Murray N., Ménard B., Thompson T. A., 2011, ApJ, 735, 66
Olsen K. P., Greve T. R., Narayanan D., Thompson R., Davé R., Rios L. N., Stawinski S., 2017, ApJ, 846, 105
Oppenheimer B. D., Davé R., 2006, MNRAS, 373, 1265
Pallottini A., Ferrara A., Gallerani S., Salvadori S., D'Odorico V., 2014a, MNRAS, 440, 2498
Pallottini A., Gallerani S., Ferrara A., 2014b, MNRAS, 444, L105
Pallottini A., Gallerani S., Ferrara A., Yue B., Vallini L., Maiolino R., Feruglio C., 2015, MNRAS, 453, 1898
Pallottini A., Ferrara A., Gallerani S., Vallini L., Maiolino R., Salvadori S., 2017, MNRAS, 465, 2540 (P17)
Pentericci L. et al., 2016, ApJ, 829, L11
Planck Collaboration XVI, 2014, A&A, 571, A16
Robertson B. E., Ellis R. S., Furlanetto S. R., Dunlop J. S., 2015, ApJ, 802, L19
Rubin K. H. R., Prochaska J. X., Koo D. C., Phillips A. C., Martin C. L., Winstrom L. O., 2014, ApJ, 794, 156
Schroetter I., Bouché N., Péroux C., Murphy M. T., Contini T., Finley H., 2015, ApJ, 804, 83
Shapley A. E., Steidel C. C., Pettini M., Adelberger K. L., 2003, ApJ, 588, 65
Shibuya T., Ouchi M., Harikane Y., 2015, ApJS, 219, 15
Steidel C. C., Erb D. K., Shapley A. E., Pettini M., Reddy N., Bogosavljević M., Rudie G. C., Rakic O., 2010, ApJ, 717, 289
Taniguchi Y. et al., 2009, ApJ, 701, 915
Teyssier R., 2002, A&A, 385, 337
Vallini L., Gallerani S., Ferrara A., Baek S., 2013, MNRAS, 433, 1567
Vallini L., Gallerani S., Ferrara A., Pallottini A., Yue B., 2015, ApJ, 813, 36
Veilleux S., Cecil G., Bland-Hawthorn J., 2005, ARA&A, 43, 769
Veilleux S. et al., 2013, ApJ, 776, 27
Verhamme A., Schaerer D., Maselli A., 2006, A&A, 460, 397
Walter F., Weiss A., Scoville N., 2002, ApJ, 580, L21
Willott C. J., Carilli C. L., Wagg J., Wang R., 2015, ApJ, 807, 180
Yue B., Ferrara A., Salvaterra R., Chen X., 2013, MNRAS, 431, 383
Yue B., Ferrara A., Pallottini A., Gallerani S., Vallini L., 2015, MNRAS, 450, 3829

This paper has been typeset from a TEX/LATEX file prepared by the author.